IMPROVED V I log(*gf*) VALUES AND ABUNDANCE DETERMINATIONS IN THE PHOTOSPHERES OF THE SUN AND METAL-POOR STAR HD 84937

J. E. Lawler[1], M. P. Wood[1], E. A. Den Hartog[1], T. Feigenson[1], C. Sneden[2], and J. J. Cowan[3]

[1] Department of Physics, University of Wisconsin, Madison, WI 53706, USA; jelawler@wisc.edu, mpwood@wisc.edu, eadenhar@wisc.edu, tfeigenson@wisc.edu
[2] Department of Astronomy and McDonald Observatory, University of Texas, Austin, TX 78712, USA; chris@verdi.as.utexas.edu
[3] Homer L. Dodge Department of Physics and Astronomy, University of Oklahoma, Norman, OK 73019, USA; cowan@nhn.ou.edu

ABSTRACT

New emission branching fraction measurements for 836 lines of the first spectrum of vanadium (V I) are determined from hollow cathode lamp spectra recorded with the National Solar Observatory 1 m Fourier transform spectrometer (FTS) and a high-resolution echelle spectrometer. The branching fractions are combined with recently published radiative lifetimes from laser-induced fluorescence measurements to determine accurate absolute atomic transition probabilities for the 836 lines. The FTS data are also used to extract new hyperfine structure *A* coefficients for 26 levels of neutral vanadium. These new laboratory data are applied to determine the V abundance in the Sun and metal-poor star HD 84937, yielding $\log \varepsilon(V) = 3.956 \pm 0.004$ ($\sigma = 0.037$) based on 93 V I lines and $\log \varepsilon(V) = 1.89 \pm 0.03$ ($\sigma = 0.07$) based on nine V I lines, respectively, using the Holweger–Müller 1D model. These new V I abundance values for the Sun and HD 84937 agree well with our earlier determinations based upon V II.

Key words: atomic data – methods: laboratory: atomic – stars: abundances – stars: individual (HD 84937) – Sun: abundances

Online-only material: color figures, machine-readable tables

1. INTRODUCTION

Studies of elemental abundances in metal-poor (old) stars provide insights on nucleosynthesis in the earliest generations of stars. Such studies have yielded large and unexpected relative iron (Fe)-group abundance trends (McWilliam et al. 1995a, 1995b; McWilliam 1997; Westin et al. 2000; Cowan et al. 2002; Sneden et al. 2003; Cayrel et al. 2004; Barklem et al. 2005; Lai et al. 2008; Bonifacio et al. 2009; Roederer 2009; Suda et al. 2011; Yong et al. 2013). The increasing role of Type Ia SNe as the Galaxy aged explains only part of the anomalous abundance trends. Relative Fe-group abundance trends can cover ±1 dex for metallicities ranging from solar ([Fe/H] ≡ 0) to −4 (e.g., Figure 12 of McWilliam 1997).[4] Better-defined abundance trends must be based on improvements in laboratory data, observations, and perhaps stellar photospheric models.

Laboratory spectroscopic data are far better now than a few decades ago due to the application of new experimental techniques and technologies (e.g., laser induced fluorescence and Fourier transform spectrometers) as well as new computational capabilities (e.g., supercomputers). Although it is now rare to find order of magnitude (1 dex) errors in experimental atomic transition probabilities, further improvements in such data are still needed in order to compare observed abundances with nucleosynthesis predictions. Studies of elemental abundances over a wide range of metallicity typically require the use of a large set of spectral lines spanning a range of wavelength, excitation potential, log(*gf*), and sometimes more than one ionization stage. There are also continuing concerns about the applicability of standard stellar photospheric models based on one-dimensional (1D) and local thermodynamic equilibrium (LTE) approximations (e.g., Asplund 2005). Such concerns grow at lower metal-

licity for several reasons. In most stars of interest, the electron pressure is provided primarily by metals and thus it decreases with metallicity. Observations also migrate toward luminous giant stars at low metallicity to capture the needed photons for high-resolution and high-S/N spectra, and the low-density atmospheres of such stars yield reduced collision rates.

Our team has started through the Fe-group neutral or first (e.g., V I) and singly ionized or second (e.g., V II) spectra with the long term goals of improving laboratory data for Fe-group elements using the best available experimental techniques and exploring the limits of standard 1D/LTE photospheric models. The existence or lack of Saha balance is of particular interest because it is thought to be a dominant non-LTE effect in stellar photospheres. The overarching objective of these studies is the mapping of the relative abundances of Fe-group elements at low metallicity. This paper complements a very recent study on V II (Wood et al. 2014a) and recent work on other spectra including Cr I (Sobeck et al. 2007), Mn I and Mn II (Den Hartog et al. 2011), Ti I (Lawler et al. 2013), Ti II (Wood et al. 2013), and Ni I (Wood et al. 2014c). In one of the earlier publications, we reported a small set of log(*gf*) values to exceptional, ±0.01 dex, accuracy and precision for Mn I and Mn II (Den Hartog et al. 2011), but we are now emphasizing larger sets of transition probabilities with somewhat larger but still tight uncertainties. Particular attention is devoted to understanding and controlling systematic errors that typically dominate transition probability uncertainties for weaker lines. We are supplementing these new transition probability data with improved isotopic and hyperfine data as needed. As a first application of these data, we are determining improved elemental abundances in the Sun and metal-poor turnoff star HD 84937.

This paper reports new absolute atomic transition probability measurements for 836 lines of V I, hyperfine structure (HFS) *A* coefficients for 26 excited levels of neutral vanadium, complete HFS line component patterns for 94 lines of V I that we find useful in abundance studies, a new solar abundance determination

---

[4] We use standard abundance notations. For elements X and Y, the relative abundances are written [X/Y] = log10(N_X/N_Y)$_{star}$ − log10(N_X/N_Y)$_{sun}$. For element X, the "absolute" abundance is written $\log \varepsilon(X) = \log_{10}(N_X/N_H) + 12$. Metallicity is defined as [Fe/H].

Table 1
Fourier Transform Spectra of a Custom Water-cooled V Hollow Cathode Discharge (HCD) Lamp

Index	Date	Serial Number	Buffer Gas	Lamp Current (mA)	Wavenumber Range (cm^{-1})	Limit of Resolution (cm^{-1})	Coadds	Beam Splitter	Filter	Detector[a]
1	1984 Dec 9	3	Ar–Ne	600	7764–49105	0.057	12	UV		Mid Range Si Diode
2	1984 Dec 9	4	Ar–Ne	300	7764–49105	0.057	8	UV		Mid Range Si Diode
3	1984 Dec 9	5	Ar–Ne	150	7764–49105	0.057	8	UV		Mid Range Si Diode
4	1986 Jul 30	9	Ar	500	14924–37018	0.048	4	UV	CuSO$_4$	Large UV Si Diode
5	1986 Jul 30	10	Ar	500	14924–37018	0.048	4	UV	CuSO$_4$	Large UV Si Diode
6	1981 Jun 16	7	Ar	332	6924–37564	0.043	8	UV	WG295	UV Mid Range Si Diode
7	1981 Jun 15	3	Ar	250	14878–36533	0.043	8	UV	CuSO$_4$ WG295	UV Mid Range Si Diode
8	1979 Dec 12	9	Ar	300	12422–31054	0.042	10	UV	TC + 4-97 WG345	Mid Range Si Diode
9	1979 Dec 12	8	Ar	300	7716–22421	0.030	8	UV	GG945	Super Blue Si Diode
10	1980 Sep 4	1	Ar	110	0–17837	0.023	5	UV	RG610	InSb
11	1983 Nov 30	3	Ar	460	2799–9518	0.011	17	CaF$_2$	Si	InSb
12	1983 Apr 17	4	Ne–Ar	370	1534–5769	0.011	80	CaF$_2$	Ge	InSb
13	1984 Jul 25	5	Ne	1000	12948–45407	0.054	8	UV	CuSO$_4$	R166 photomultiplier Mid Range Si Diode
14	1983 Nov 30	4	Ne	510	2799–9517	0.011	16	CaF$_2$	Si	InSb

Notes. All spectra were recorded using the 1 m FTS on the McMath telescope at the National Solar Observatory, Kitt Peak, AZ.
[a] Detector types include the Super Blue silicon (Si) photodiode, Large UV Si photodiode, Mid Range Si photodiode, UV Mid Range Si photodiode, a solar blind R166 photomulitplier, and InSb detectors for the IR. The UV beam splitter is fused silica.

of $\log \varepsilon(V) = 3.956 \pm 0.004$ ($\sigma = 0.037$) based on 93 transitions of V I, and a new abundance determination in HD 84937 of $\log \varepsilon(V) = 1.89 \pm 0.03$ ($\sigma = 0.07$) based on nine transitions of V I using the Holweger–Müller 1D model. The HFS line component patterns for 94 transitions are based on a combination of our new HFS A coefficients and the best published HFS coefficients. The new transition probabilities are put on a highly reliable absolute scale using radiative lifetimes from laser induced fluorescence (LIF) measurements (Den Hartog et al. 2014) of the upper levels for all 836 transitions. The transition probability and HFS line component patterns are all in machine-readable tables to support continuing studies of metal-poor stars.

2. BRANCHING FRACTION MEASUREMENTS FOR V I LINES

Data from two complementary spectrometers are used in this work on V I and in recent work on V II (Wood et al. 2014a). One of these is the venerable National Solar Observatory (NSO) 1 m Fourier transform spectrometer (FTS) developed for the McMath Solar telescope on Kitt Peak, AZ (Brault 1976). Although the NSO 1 m FTS is no longer in service, all of the data recorded using the instrument are still available through the electronic archives of the NSO.[5] These spectroscopic data, including the laboratory data, are of great value due to the exceptional resolving power and absolute wavenumber accuracy of the NSO 1 m FTS. These performance features of the 1m FTS are critical in studies of dense spectra from rare earth elements (e.g., Lawler et al. 2009; Sneden et al. 2009). The broad spectral coverage and parallel data collection of an interferometric spectrometer makes the FTS data even more valuable for branching fraction determinations. Branching fraction errors from drifts in a source are minimized if a spectrometer simultaneously records all spectral resolution elements over a broad spectral region. Wood et al. (2014a) used 13 archived spectra during work on V II and these spectra are also used here with one additional infrared (IR) FTS spectrum from the NSO electronic archives.

The second instrument is the 3 m focal length echelle spectrometer at the Univ. of Wisconsin (Wood & Lawler 2012). This instrument was developed to complement the NSO 1 m FTS. The primary advantages of the 3 m echelle over the FTS are its superior UV sensitivity and lack of multiplex noise. Multiplex noise is the smooth redistribution of quantum statistical (Poisson) noise inherent to interferometric spectrometers. The primary disadvantages of the 3 m echelle compared to the NSO 1 m FTS are the slightly lower spectral resolving power of $\lambda/\Delta\lambda = 250,000$ and the less accurate wavelengths or wavenumbers of a dispersive spectrometer. These disadvantages are tolerable in studies of Fe-group or simpler spectra, and the advantages are critical for measuring weak UV lines.

Table 1 lists the 14 spectra from the NSO 1 m FTS. Table 2 lists the spectra from the 3 m echelle spectrometer used in this V I study. The list of echelle spectra is also somewhat expanded from the list of spectra used by Wood et al. (2014a) in recent work on V II. A set of echelle spectra (#107–126 in Table 2) of a custom water-cooled hollow cathode lamp running with discharge currents from 32 mA to 50 mA is added to pick up some additional UV lines of V I. Spectra in both lists are from low-pressure hollow cathode lamps, which yield very narrow lines from sputtered metal. It is always important to use a large set of spectra recorded with a range of lamp currents in branching fraction studies. This makes it possible to eliminate optical depth errors and to identify and correct more line blends including blends between neutral atom and ion lines of the metal, blends between metal lines and buffer gas lines, and sometimes even blends between pairs of metal lines from the same ionization stage. Optical depth errors and the first two types of blends have distinct and easily recognized current dependence in branching fraction measurements. Optical depth problems are less severe in V I than in recent work on Ni I (Wood et al. 2014c): in fact spectrum #7 in Table 1 is optically thin to a good approximation for all lines of V I. We use echelle data at low lamp current to test for optical depth problems. The HFS of V I lines is at least part of the reason for less serious optical depth problems compared to Ni I.

Branching fraction measurements are attempted for all 168 levels of neutral vanadium with radiative lifetimes measured by

---

[5] http://diglib.nso.edu/

Table 2
Echelle Spectra of Commercial V HCD Lamps and A Custom Water-cooled V HCD Lamp

Index	Date	Serial Numbers[a]	Buffer Gas	Lamp Current (mA)	Wavelength Range (Å)	Resolving Power	Coadds	Exposure Time (s)
47–51	2013 May 24	1, 3, 5, 7, 9	Ne	3	2200–3900	250,000	60	90
52–56	2013 May 21	1, 3, 5, 7, 9	Ne	5	2200–3900	250,000	90	60
57–61	2013 May 22	1, 3, 5, 7, 9	Ne	10	2200–3900	250,000	90	60
62–66	2013 May 23	1, 3, 5, 7, 9	Ne	15	2200–3900	250,000	60	90
67–71	2013 May 20	1, 3, 5, 7, 9	Ar	3	2200–3900	250,000	6	900
72–76	2013 May 15	1, 3, 5, 7, 9	Ar	5	2200–3900	250,000	18	300
77–81	2013 May 16	1, 3, 5, 7, 9	Ar	10	2200–3900	250,000	88	60
82–86	2013 May 17	1, 3, 5, 7, 9	Ar	12	2200–3900	250,000	60	90
87–91	2014 Jan 30	1, 3, 5, 7, 9	Ne	5	2000–2800	250,000	18	300
92–96	2014 Jan 31	1, 3, 5, 7, 9	Ne	10	2000–2800	250,000	36	150
97–101	2014 Feb 3	1, 3, 5, 7, 9	Ne	15	2000–2800	250,000	72	75
102–106	2014 Feb 5	1, 3, 5, 7, 9	Ar	15	2000–2800	250,000	45	120
107–111	2014 Apr 24	1, 3, 5, 7, 9	Ar	32	2100–3200	250,000	30	120
112–116	2014 Apr 16	1, 3, 5, 7, 9	Ar	40	2100–3200	250,000	20	180
117–121	2014 Apr 17	1, 3, 5, 7, 9	Ar	40	2100–3200	250,000	20	180
122–126	2014 Apr 28	1, 3, 5, 7, 9	Ar	50	2100–3200	250,000	20	180
127–131	2014 May 13	1, 3, 5, 7, 9	Ar	10	2100–3200	250,000	40	180
132–136	2014 May 9	1, 3, 5, 7, 9	Ar	15	2100–3200	250,000	90	60
137–141	2014 May 14	1, 3, 5, 7, 9	Ne	15	2100–3200	250,000	120	45

Notes. [a] At least three CCD frames are needed to capture a complete echelle grating order in the UV. In the above data, five CCD frames are used to provide redundancy and a check for lamp drift.

Den Hartog et al. (2014) and completed for 144 upper levels. The remaining levels have difficult-to-separate blending issues on one or more strong branches or other similar problems with UV lines that appear only in our echelle spectra. Improved energy levels from Thorne et al. (2011) are used to evaluate the wavenumber of every possible transition satisfying the parity change and $|\Delta J| \leqslant 1$ selection rules from the upper levels of interest. The $|\Delta L| \leqslant 1$ and $\Delta S = 0$ selection rules of LS or Russell–Saunders coupling are violated by many weak transitions of Fe-group and heavier species. Weak transitions are often important in studies on high abundance Fe-group elements. Interactive computer programs are used to set baselines and integration limits for numerical integration of transitions in the FTS and echelle data. Too many of the HFS coefficients for levels of V I are still unknown to use line profile fitting to evaluate the strength of transitions in the FTS data, and the echelle data do not have high enough resolving power to justify such profile fitting.

Several blends of V I and V II lines are separated using the current dependence of the total integrated feature (e.g., Lawler et al. 2011). Blends of pairs of V I lines are most conveniently separated in FTS data using the accurate energy levels reported by Thorne et al. (2011). This involves using Ritz wavenumbers for the blended transitions and requiring that a normalized and weighted combination of the Ritz wavenumbers match the center-of-gravity of the blended feature. This also works for blends of V I and V II lines in FTS data using the accurate energy levels for V II from Thorne et al. (2013). Echelle data generally do not have sufficiently accurate wavelengths or wavenumbers for these blend separation techniques based on Ritz wavenumbers to be utilized.

A relative radiometric calibration is essential to convert the above transition strengths from numerical integration into strengths proportional to photons per unit time. The relative calibration of the FTS is determined using sets of known Ar I and Ar II branching ratios established and checked by Adams & Whaling (1981), Danzmann & Kock (1982), Hashiguchi &

Hasikuni (1985), and Whaling et al. (1993). This calibration method is best suited to FTS data from hollow cathode lamps with Ar as a buffer gas and the technique is internal to the spectra. It captures transmission and reflection of all surfaces in the optical train including the lamp window and internal metal surfaces of the lamp cathode that might reflect or scatter light. Often FTS mirror alignment drifts very slightly (a small fraction of a wavelength) while many interferograms are recorded and co-added. The subtle alignment drift first changes UV roll-off of sensitivity but the internal Ar I and Ar II calibration captures any change in UV roll-off. This widely used Ar I and Ar II branching ratio technique extends from the IR to about 35,000 cm^{-1} or 2800 Å in the UV. Although it is tempting to use continuum standard lamps to calibrate the 1m FTS in the UV, this approach is very difficult to implement in the UV. Spectral ghosts in the FTS output are at least part of the difficulty, because the ghost of a continuum is a continuum and indistinguishable from the desired calibration signal.

The relative radiometric calibration of the echelle spectrometer is from NIST traceable D$_2$ lamp spectra recorded immediately after each hollow cathode CCD frame. Calibrated D$_2$ lamps are convenient radiometric standards, but they age from color center formation in their exit window. In branching fraction studies, absolute radiometric calibrations are not necessary, but unfortunately color center formation can yield a somewhat wavelength dependent loss of transmission. The "everyday" D$_2$ lamp is periodically checked against another NIST-traceable D$_2$ lamp that has far fewer hours of operation, and against a windowless Ar miniarc (Bridges & Ott 1977) calibrated directly by Bridges at NIST. The D$_2$ lamp calibrations of the echelle extend from about 25,000 cm^{-1} or 4000 Å to about 50,000 cm^{-1} or 2000 Å. The echelle data are primarily used in the UV to provide better sensitivity, test for optical depth errors, and serve as a redundant calibration.

Often a correction for "residuals" or unobserved lines is performed in branching fraction studies. The energy level structure of neutral vanadium is now known well enough that

Table 3
Experimental Atomic Transition Probabilities for 836 Lines of V I Organized by Increasing Wavelength in Air

Wavelength in Air[a]	Upper Level			Lower Level			Transition Probability	log(gf)
(Å)	Energy[b] (cm^{-1})	Parity	J	Energy[b] (cm^{-1})	Parity	J	$(10^6 \ s^{-1})$	
2384.287	41928.473	od	0.5	0.000	ev	1.5	4.9 ± 0.5	−2.08
2401.904	41758.357	od	3.5	137.383	ev	2.5	8.6 ± 1.6	−1.22
2406.748	41860.647	od	4.5	323.432	ev	3.5	9.4 ± 1.6	−1.09
2412.690	41758.357	od	3.5	323.432	ev	3.5	10.8 ± 2.1	−1.12
2420.121	41860.647	od	4.5	552.955	ev	4.5	10 ± 1.7	−1.06

Notes.

[a] Wavelength values computed from energy levels using the standard index of air from Peck & Reeder (1972).

[b] Energy levels are from Thorne et al. (2011).

(This table is available in its entirety in a machine-readable form in the online journal. A portion is shown here for guidance regarding its form and content.)

transitions to "unobserved" lower levels are not a concern. The term unobserved rather than "unknown" is preferred to describe levels that are predicted to exist in a certain energy range but have not yet been observed. While such unobserved levels exist in some rare earth atoms and ions even at fairly low excitation energies and can be a problem, this is not a concern in work on V I. There is also a possibility of weak branches in the optical or UV dropping below the multiplex noise floor in FTS data. However, a set of FTS spectra like that in Table 1, can be used to measure branching fractions as small as a few times 0.0001. This typically involves "bootstrapping" intensity ratios of transitions connected to a common upper level from high current spectra to progressively lower current spectra due to optical depth issues.

The most serious potential sources of residuals in our work on V I are IR lines. Upper levels with short radiative lifetimes due to strong optical and UV branches rarely have significant IR branches. The frequency cubed scaling of an Einstein A coefficient for a fixed dipole matrix element suppresses IR branching fractions. One must keep in mind that the IR branches can be important for other reasons even if they do not affect the accuracy of optical or UV branching fractions. For example, the Ti II line in the H band studied recently by Wood et al. (2014b) has a rather small branching fraction <0.0005 but is valuable to the Sloan Digital Sky Survey (SDSS) III Apache Point Observatory Galactic Evolution Experiment (APOGEE). Titanium may be the only element with the combination of good neutral lines and an ion line in the H band. The increasing availability and size of HgCdTe detector arrays is having a huge impact on IR astronomy from the ground and space.

Spectra 10–12 and 14 of Table 1 were recorded using InSb detectors and they provide good IR coverage, which unfortunately has limited overlap with spectra recorded using Si detectors. In order to measure reliable IR branching fractions, the upper level of interest needs a transition around 9000 or 10,000 cm^{-1} with good S/N in both the optical-UV spectra recorded using a Si detector and the IR spectra. Low-pressure hollow cathode lamps are not LTE sources, and thus upper level populations vary from level-to-level in an unpredictable fashion and do not in general have a uniform dependence on lamp current. Lines used to "bridge" intensity ratios from optical–UV spectra to IR spectra must be found for each upper level of interest. Another method is to rely on theory to make a small correction for IR branches from levels with radiative lifetimes >100 ns. We use the online Kurucz (2011) database[6] to include corrections to the optical branching fractions from levels of the z^4G term due to IR branches. The multiplicative corrections

range from 0.922 to 0.946. Similar corrections of 0.932 to 0.941 are made for lines from levels of the z^4F term. The Kurucz database is examined for many other relatively long lived levels, including the z^6D with radiative lifetimes of ~400 ns, but IR branches are found to be negligible, ⩽0.01.

Uncertainties on final average branching fractions are evaluated using the strength of the branching fraction, the S/N of the data, and the wavenumber separation of lines from the common upper level. Uncertainty always migrates to the weaker branches. As in past work we estimate the calibration uncertainty to be 0.001%/cm^{-1} (Wickliffe et al. 2000). This calibration uncertainty is combined with the standard deviation of results from multiple spectra to determine the branching fraction uncertainty.

3. V I TRANSITION PROBABILITIES AND COMPARISON TO EARLIER MEASUREMENTS

Transition probabilities are given in Table 3 for 836 lines of V I. Lifetimes from Den Hartog et al. (2014) are used to establish the absolute scale and convert the emission branching fractions described in the preceding section into accurate absolute Einstein A coefficients. A comparison between results of Den Hartog et al. and earlier results show excellent agreement with the works of Whaling et al. (1985) −0.2% mean and 0.6% rms in the sense (old − new)/new for 39 lifetimes in common, Doerr et al. (1985) −0.8% mean and 0.8% rms for 12 lifetimes in common, and Xu et al. (2006) −0.2% mean and 0.9% rms for 10 lifetimes in common. Good agreement, +4.7% mean and 1.8% rms, is found in a comparison to early results by Rudolph & Helbig (1982) for nine lifetimes in common. Uncertainties on the transition probabilities are simply the branching fraction uncertainty combined in quadrature with the radiative lifetime uncertainty of ±5% from Den Hartog et al. (2014). Energy levels are from Thorne et al. (2011) and wavelengths are computed using energy level differences and the standard refractive index of air (Peck & Reeder 1972). The sums of the transition probabilities for lines connected to the upper levels of the z^4G and z^4F terms are less than the inverse of the upper level lifetimes due to the residual corrections discussed in Section 2. The sums of the transition probabilities for lines connected to some other upper levels are also less than the inverse of the upper level lifetimes, typically by a few percent, due to weak transitions that have been omitted from Table 3 but kept in the branching fraction normalization. Such weak lines are omitted due to ambiguous classifications, obvious blending, or poor S/N, but they have little effect on the transition probabilities in Table 3 and almost no effect on the transition probability uncertainties in Table 3.

---

[6] http://www.cfa.harvard.edu/amp/ampdata/kurucz23/sekur.html

An important set of comparisons between our atomic transition probability measurements and earlier work is based on the online NIST Atomic Spectra Database (ASD; Kramida et al. 2013). Transition probabilities in this database are critically compiled and thus based on the best available results with periodic updates. Accuracy in the NIST ASD is ranked using an A, B, C, D, E scheme where A is $\leqslant \pm 3\%$, B is $\leqslant \pm 10\%$, C is $\leqslant \pm 25\%$, D is $\leqslant \pm 50\%$, and E is $> \pm 50\%$ with occasional $+$ notation (e.g., C+ to indicate uncertainties between B and C). There are no A-rated NIST data for V I. Figures 1(a) and (b) are comparisons of our measurements to ASD V I data with B and B+ ratings as a function of wavelength and as a function of our log(gf) value for 147 lines in common. On close inspection all of the combined B and B+ rated NIST results are from Whaling et al. (1985). These authors used the same method employed here, combining radiative lifetimes from LIF measurements with branching fractions from FTS spectra. We use independent radiative lifetime measurements (Den Hartog et al. 2014) but we probably use the FTS spectrum employed by Whaling et al. We also use many additional spectra from the NSO 1 m FTS electronic archives and supplementary data from our echelle spectrometer at shorter wavelengths. Whaling et al. wrote "Most of the lines were measured on a single spectrum covering the range 3000–10,000 Å, with the FTS parameters set to give a resolution of 8.7×10^5." Based on the date of the paper and the resolving power of the spectrum, we think that spectrum 6 of Table 1 was used by Whaling et al.

There are numerous inconsistencies between the branching fractions (BFs) and transition probabilities in Table 2 of Whaling et al. (1985). The most serious inconsistencies are in the last section of Table 2 covering lines from the x^{4}G upper levels. The transition probabilities of the lines from the x^{4}G levels are a factor of 100 too small, likely due to an error in the column header. In the main body of Table 2 Whaling et al. have an inconsistency of an order of magnitude between the BF and transition probability for the line at 5761.426 Å from the upper level at 25930.544 cm^{-1}. NIST compilers renormalized all transition probabilities from the x^{4}G levels and the level at 25930.544 cm^{-1}. Figures 1(a) and (b) includes the recommended log(gf) values in the NIST ASD except for the omission of the line 5761.426 Å which disagrees with our value by nearly 1 dex. The outlier in Figure 1(a) at 3784.669 Å is a minor BF $<$ 0.001 transition but spectra 1 through 7 of our study yield a consistent result and thus we are confident in our value.

Scott et al. (2014) note that other lines in Table 2 of Whaling et al. have non-negligible inconsistencies between BFs and transition probabilities. It is difficult to correct these problems because it is not clear whether the BF (e.g., lines from the x^{4}G levels) or transition probability (e.g., 5761.426 Å) in Table 2 of Whaling et al. is the intended and perhaps better result. Figure 1(c) includes a BF comparison for the same 147 lines ranked B and B+ by NIST in common between Whaling et al. and our experiment.

Figures 2(a) and (b) are comparisons of our measurements to NIST ASD V I data with combined C and C+ ratings as a function of wavelength and as a function of our log(gf) value for 227 lines in common. The C and C+ NIST ASD transition probabilities include some of the less accurate results from Whaling et al. (1985) as well as older relative measurements from King (1947) and from Ostrovskii & Penkin (1958). These older relative measurements were put on an absolute scale by NIST compilers using more recent lifetime measurements. The comparisons in Figures 2(a) and (b) are not as good as those of
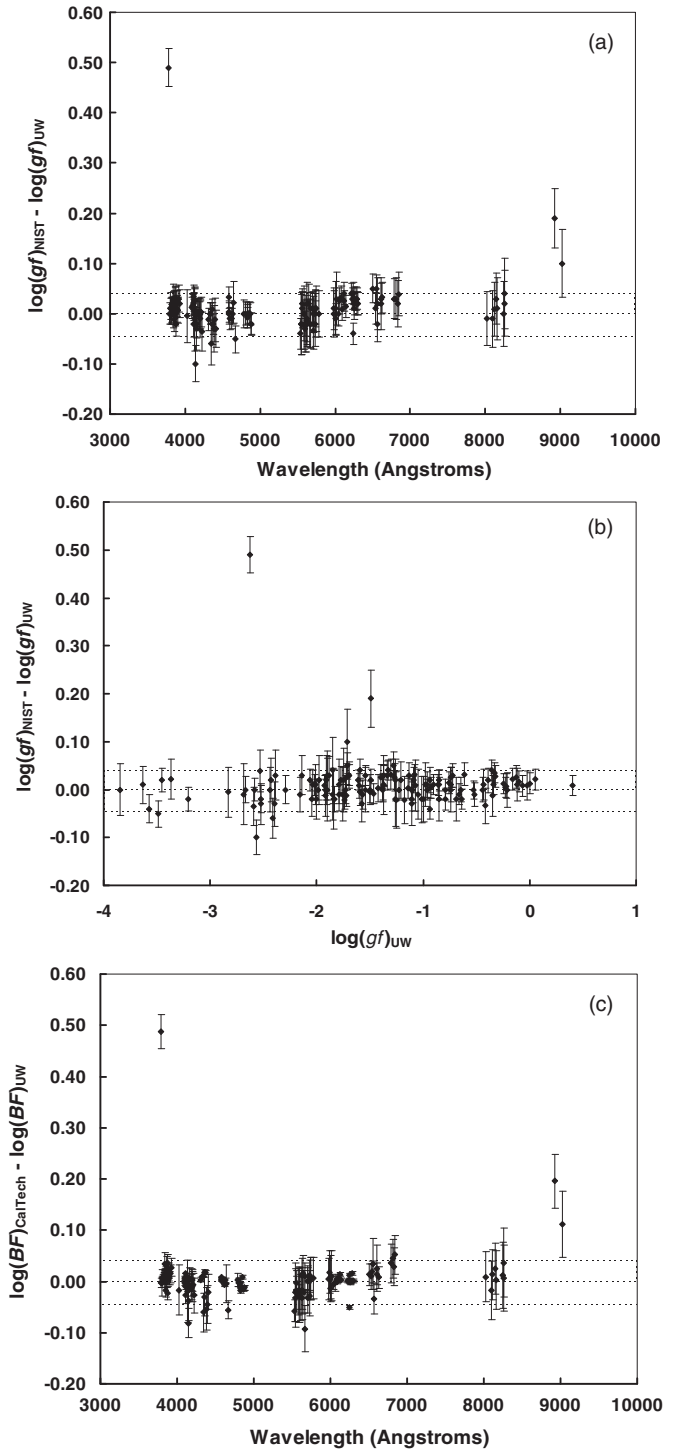
Figure 1. (a) Comparison of our (UW) log(gf) values for 147 lines to NIST values with accuracy rating "B" ($\leqslant 10\%$) and "B+" in the NIST database as a function of wavelength. The central dotted line indicates perfect agreement. The upper and lower dotted lines denote $\pm 10\%$ differences. Error bars on the data points are from our measurements. (b) Same as (a) except plotted as a function of our log(gf). (c) Similar to (a) except branching fractions BF$_{CalTech}$ from Whaling et al. (1985) are compared to our branching fractions BF$_{UW}$.

Figure 1. Using only Figure 2(a) one might conclude that either the NIST ASD data or our data has a wavelength dependent error. However, using Figure 2(b), it is apparent that stronger lines are responsible for most of the discordance in Figure 2(a). Uncertainties or errors in transition probabilities of stronger lines are primarily due to the normalization. The lifetimes used
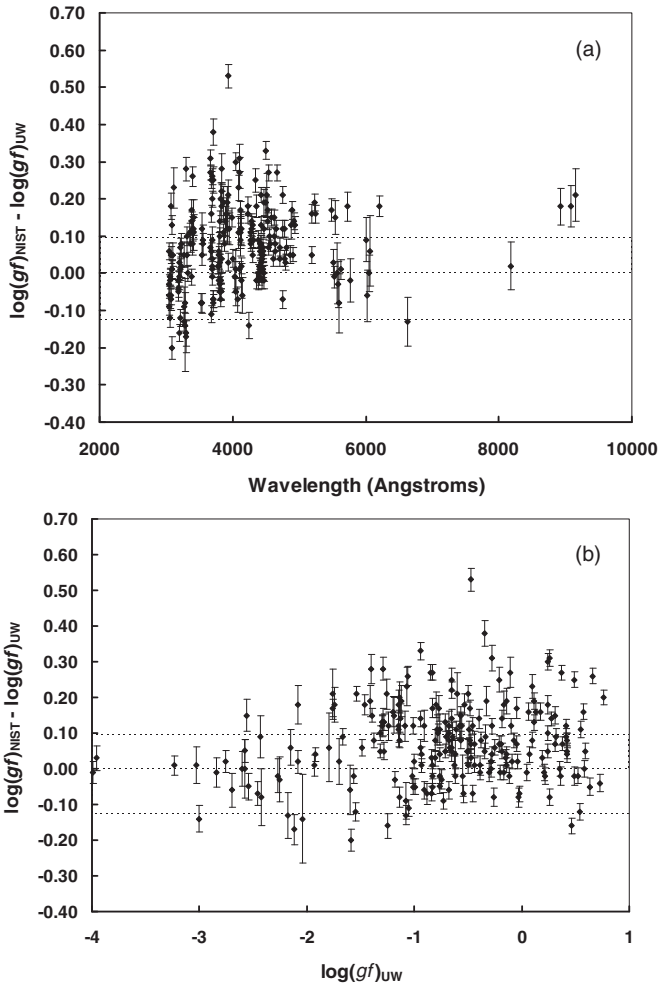
Figure 2. (a) Comparison of our (UW) log(*gf*) values for 227 lines to NIST values with accuracy rating "C" (⩽25%) and "C +" in the NIST database as a function of wavelength. The central dotted line indicates perfect agreement. The upper and lower dotted lines denote ±25% differences. Error bars on the data points are from our measurements. (b) Same as (a) except plotted as a function of our log(*gf*).

to normalize our log(*gf*) values from each upper level from Den Hartog et al. (2014) contribute only ±0.02 dex to our log(*gf*) uncertainties. In addition to the accurate radiative lifetimes used for normalization, we have confidence in our results for other reasons. We use much more FTS data, as well as echelle data in our branching fraction measurements than was used in earlier studies. This has advantages in understanding and controlling systematic errors, e.g., variations of a branching fraction as a function of current can reveal hidden blends. Hidden blends between V I and V II lines have distinct current dependence as do hidden blends with buffer gas lines. Even blends between pairs of V I lines or pairs of V II lines are often separable now that the energy levels of neutral and singly ionized vanadium are accurately known (Thorne et al. 2011, 2013).

There are 14 additional lines in common between this study and the NIST ASD that have accuracy ratings of D or E. These data are from the publications referenced above, these data agree with our data to within the combined uncertainties.

4. HYPERFINE STRUCTURE

Data on hyperfine structure (HFS) is necessary for accurate and precise abundance studies, especially for elements like

vanadium with odd-*Z* (an unpaired proton). Isotopes of even-*Z* elements with an unpaired neutron also have HFS. Knowledge of the HFS component patterns is important in syntheses of blended or poorly resolved lines. Such knowledge is also important for "de-saturating" strong lines. Vanadium in the solar system is more than 99.7% ^{51}V with a nuclear spin $I = 7/2$.

Numerous studies of the HFS in V I have been published and our review of these papers indicates that the work is all of at least good quality with reasonable uncertainty estimates. Childs and Goodman (1967) used radio frequency (RF) spectroscopy to study the HFS of levels in the two lowest terms of ^{51}V I. Their HFS *A* (magnetic dipole) and *B* (electric quadrupole) coefficient measurements have sub kHz uncertainties and are still the most accurate available for the lowest levels of ^{51}V I. We use the Casimir formula as presented in the elementary text by Woodgate (1980)

$$\Delta E = \frac{AK}{2} + B\frac{3K(K+1) - 4I(I+1)J(J+1)}{8I(2I-1)J(2J-1)},$$

where ΔE is the shift in wavenumbers of an HFS sub-level (*F, J*) from the center of gravity of the fine structure level (*J*),

$$K = F(F+1) - J(J+1) - I(I+1),$$

F is the total atomic angular momentum, *J* is the total electronic angular momentum, and *I* is the nuclear spin. Childs & Goodman (1967) attempted to determine HFS *C* (magnetic octupole) coefficients but reported values with uncertainties overlapping zero. The *A, B, C* expansion of HFS interactions converges rapidly. In this work we use the best available published *B* coefficients, but we have not attempted to determine additional *B* coefficients. Gough et al. (1985) used a single-frequency laser to study a multiplet from the ground 3d^4(^{5}D)4s a^{6}D term to the excited 3d^4(^{5}D)4p z^{6}D^o term. Their measurements are quite good, but have since been superseded by the single frequency laser measurements of Cochrane et al. (1998). Single-frequency laser measurements of HFS *A* and *B* coefficients routinely have sub MHz accuracy.

Knowledge of a limited number of HFS *A* coefficients with very good precision and accuracy can be combined with spectral line profiles in FTS data to extract HFS *A* coefficients for many additional levels. FTS instruments provide far greater spectral coverage than single-frequency lasers. Although some HFS *B* coefficients are known for the lowest levels of V I, it is typically not possible to get reliable HFS *B* coefficients from least-square fits to partially resolved HFS patterns in FTS data. Palmeri et al. (1995, 1997) and Lefèbvre et al. (2002) used FTS data to extract HFS *A* coefficients for many additional levels. More recently, Güzelçimen et al. (2011) determined the HFS *A* coefficients for the levels of the lowest odd parity term of V I using FTS data. We have expanded the above FTS measurements to obtain HFS *A* coefficients for 26 additional levels as reported in Table 4. The best of the above mentioned HFS data combined with our new measurements are used to generate complete HFS component patterns for 94 lines of ^{51}V I in Table 5. Many of the 94 lines in Table 5 have non-negligible HFS and are quite useful for abundance determinations in the Sun and HD 84937. Useful in this sense means that a reliable log(*gf*) is available and the line is relatively unblended with a well-defined continuum level. Modern spectral synthesis techniques broaden the definition of a useful line. Many other lines of V I with negligible HFS, as can be verified from inspection of FTS data, are also useful.

Table 4
Hyperfine Structure (HFS) A Coefficients for 25 Odd Parity
Levels and One Even Parity Level of Neutral Vanadium from
Least-square Fits to Line Profiles in FTS Data

| Configuration	Term	J	Level Energy[a] (cm^{-1})	HFS A Coefficient (mK)
3d^4(^{5}D)4p	z^{4}P°	1/2	24770.673	−26.6
3d^4(^{5}D)4p	z^{4}P°	3/2	24915.151	−9.7
3d^4(^{5}D)4p	z^{4}P°	5/2	25131.002	−3.1
3d^4(^{5}D)4p	y^{6}F°	5/2	24898.804	3.3
3d^4(^{5}D)4p	y^{6}F°	7/2	24992.909	2.5
3d^4(^{5}D)4p	y^{6}F°	9/2	25111.473	2.1
3d^4(^{5}D)4p	y^{6}F°	11/2	25253.457	2.0
3d^4(^{5}D)4p	y^{6}D°	5/2	26505.953	0.5
3d^4(^{5}D)4p	y^{6}D°	7/2	26604.807	1.9
3d^4(^{5}D)4p	y^{6}D°	9/2	26738.323	3.1
3d^3(^{4}P)4s4p(^{3}P)	y^{6}P°	3/2	29202.790	18.0
3d^3(^{4}P)4s4p(^{3}P)	y^{6}P°	5/2	29296.430	13.0
3d^3(^{4}P)4s4p(^{3}P)	y^{6}P°	7/2	29418.119	15.2
3d^3(^{4}F)4s4p(^{1}P)	x^{4}G°	5/2	31397.822	20.1
3d^3(^{4}F)4s4p(^{1}P)	x^{4}G°	7/2	31541.167	9.7
3d^3(^{4}F)4s4p(^{1}P)	x^{4}G°	9/2	31721.780	5.3
3d^3(^{4}F)4s4p(^{1}P)	x^{4}G°	11/2	31937.131	2.7
3d^3(^{4}F)4s4p(^{1}P)	w^{4}F°	5/2	32846.822	8.6
3d^3(^{4}F)4s4p(^{1}P)	w^{4}F°	7/2	32988.845	3.6
3d^4(^{3}H)4p	z^{4}I°	15/2	37518.445	6.1
3d^4(a^{3}P)4p	t^{4}D°	3/2	37835.065	7.1
3d^4(a^{3}P)4p	t^{4}D°	7/2	38115.684	4.8
3d^4(^{3}H)4p	x^{2}H°	9/2	38123.795	10.0
3d^4(^{3}H)4p	x^{2}H°	11/2	38220.663	10.4
3d^4(a^{3}F)4p	u^{4}F°	9/2	39391.079	9.5
3d^{3}4s(^{5}F)5s	e^{6}F	11/2	37931.460	21.1

Notes. The best results from earlier studies described in the text are constrained in the least-square fits. Uncertainties are ±1 mK (±0.001 cm^{-1}) except for levels at 29202.790 and 29296.430 that are each determined using one infrared line. The HFS A coefficients for these two levels have uncertainties of ±2 mK.
[a] Thorne et al. (2011).

5. THE VANADIUM ABUNDANCE IN THE SOLAR PHOTOSPHERE

We use our V I transition probability and HFS data to derive a new V abundance for the solar photosphere. We follow closely the methods of our previous studies of Fe-group species: Ti I (Lawler et al. 2013), Ti II (Wood et al. 2013), Ni I (Wood et al. 2014c) and V II (Wood et al. 2014a). A summary is given here, and the reader is referred to the previous papers for details.

We first estimate relative V I transition strengths with the simple formula

$$STR \equiv \log(gf) - \theta\chi.$$
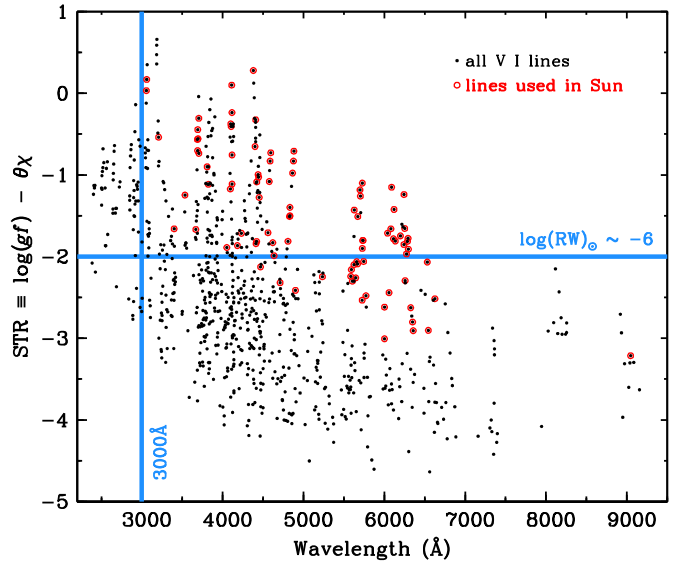
Figure 3. Relative strengths of V I lines STR plotted as functions of line wavelength; see text for further discussion. The vertical blue line indicates the atmospheric cutoff for ground-based spectroscopy. The horizontal blue line indicates the STR values of very weak lines (reduced widths log(RW) = −6). Red circles are for the lines of our solar analysis.

(A color version of this figure is available in the online journal.)

The log(gf) values and excitation energies χ (converted to units of eV) are given in Table 3, and for this rough calculation we assume an inverse temperature $\theta = 5040/T \approx 1.0$. The STR values are plotted as a function of wavelength in Figure 3. Red circles are used to indicate the lines that are employed in our solar analysis. The line at STR = −2.0 indicates the strengths of V I lines which are very weak in the solar spectrum. With reduced width defined with respect to equivalent width (EW) as log(RW) = log(EW/λ), a strength of STR ∼ −2 corresponds to log(RW) ∼ −6 (EW ∼ 5 mÅ at 5000 Å) in the solar center-of-disk spectrum (Delbouille et al. 1973).[7] If such lines are unblended, they are potentially useful photospheric vanadium abundance indicators. Inspection of Figure 3 shows that we were able to use some lines as weak as STR ∼ −3, or log(RW) ∼ −7 (EW < 1 mÅ) in our analysis. This is possible because they occur mostly in the wavelength range 5500–6500 Å, where the contamination by other atomic species and (especially) CN is small in the solar spectrum.

For each of the 836 transitions in Table 3 we begin with consideration of its potential usefulness by consulting the

---
7 http://bass2000.obspm.fr/solar_spect.php

Table 5
Hyperfine Structure (HFS) Line Component Patterns for 94 Transitions of ^{51}V I Computed from the Best Published HFS Coefficients (See Text) and
New HFS A Coefficients of Table 4, Energy Levels of Thorne et al. (2011), and the Standard Index of Air (Peck and Reeder 1972)

Transition Wavenumber (cm^{-1})	Wavelength in Air (Å)	F_{upp}	F_{low}	Component Position (cm^{-1})	Component Position (Å)	Strength Normalized to 1.0 for Each Transition
32709.439	3056.333	6	6	−0.01853	0.001732	0.22569
32709.439	3056.333	6	5	0.04581	−0.004281	0.04514
32709.439	3056.333	5	6	−0.07013	0.006554	0.04514
32709.439	3056.333	5	5	−0.00579	0.000541	0.11546
32709.439	3056.333	5	4	0.04779	−0.004466	0.06857

Notes. Center-of-gravity wavenumbers and air wavelengths are given with component positions relative to those values.

(This table is available in its entirety in a machine-readable form in the online journal. A portion is shown here for guidance regarding its form and content.)

7

Delbouille et al. (1973) photospheric spectrum, the Moore et al. (1966) solar line identifications, and the Kurucz (2011)[8] atomic/molecular line database. This results in the elimination of almost all lines with STR < -3, and many more lines that are severely blended with other spectral features. For all surviving V I transitions, we compute synthetic spectra with the current version of the LTE line analysis code MOOG (Sneden 1973). Lawler et al. (2013) describe assembly of the line lists. We start with the Kurucz (2011) line database, gathering atomic and C_2, CH, CN, NH, OH, and MgH molecular lines in a small spectral interval (typically 4 Å) centered on each V I line. We then modify transition probabilities and account for isotopic/hyperfine substructure from recent lab studies on these species: ionized rare earths (Sneden et al. 2009 and references therein), Ti I (Lawler et al. 2013), Ti II (Wood et al. 2013), V II (Wood et al. 2014a), Cr I (Sobeck et al. 2007), Ni I (Wood et al. 2014c). Much of the molecular data come from recent lab investigations: C_2, Brooke et al. (2013) and Ram et al. (2014); CH, Masseron et al. (2014); CN, Brooke et al. (2014) and Sneden et al. (2014); MgH, GharibNezhad et al. (2013) and Hinkle et al. (2013). The data for NH and OH are obtained from Kurucz (2011).

To be consistent with our previous work beginning with Lawler et al. (2001), we adopt the Holweger & Müller (1974) empirical model photosphere. Raw synthetic spectra are computed by MOOG with this model and the linelists described above, and convolved empirically with Gaussian smoothing functions to account for the (very narrow) spectrograph instrument profile and solar macroturbulence. The data for atomic and molecular lines with recent lab transition probabilities, hyperfine substructures, and isotopic wavelength shifts are adopted without change. The $>99.7\%$ abundance of ^{51}V eliminates the need for vanadium isotopic shifts. For other contaminants, we adjust their log(gf) values to match the observed solar spectrum.

Inspection of observed/synthetic solar spectrum matches lead to elimination of more V I line candidates due to unacceptable contamination by other species or extreme line weakness of the V I transition. Of the 836 lines with new log(gf) values given in Table 3, only 93 survive to be used in our solar abundance analysis. This factor of 10 winnowing is due to two effects. First, V has a relatively modest abundance compared to other Fe-group elements. In the atomic number range $21 \leqslant Z \leqslant 30$, V has the second smallest solar abundance, $\log \varepsilon(V) \sim 4.0$. All but two of the other Fe-group elements are more abundant by >0.5 dex. Second, V is almost completely ionized in the Sun; the V I number densities thus are very small. These effects combine to make the majority of V I lines very weak (log(RW) $\leqslant -6$; see Figure 3).

For the majority of usable solar V I lines, derivation of accurate abundances require application of the hyperfine substructures discussed in Section 4. In Figure 4, we show two examples of lines with wide hyperfine splitting. The 4379.23 Å line shown in panel (a) is one of the strongest V I transitions (STR = 0.28; see Figure 3) and remains saturated even when spread into its 21 subcomponents. The 5731.25 Å is far weaker, EW = 9.0 mÅ (RW = -5.80, STR = -1.80), and can potentially be treated as a single line in an EW matching analysis. However, inspection of the profile of this line in panel (b) reveals a non-Gaussian shape; only direct integration methods can yield an accurate EW for this and other lines that have significant hyperfine substructure.
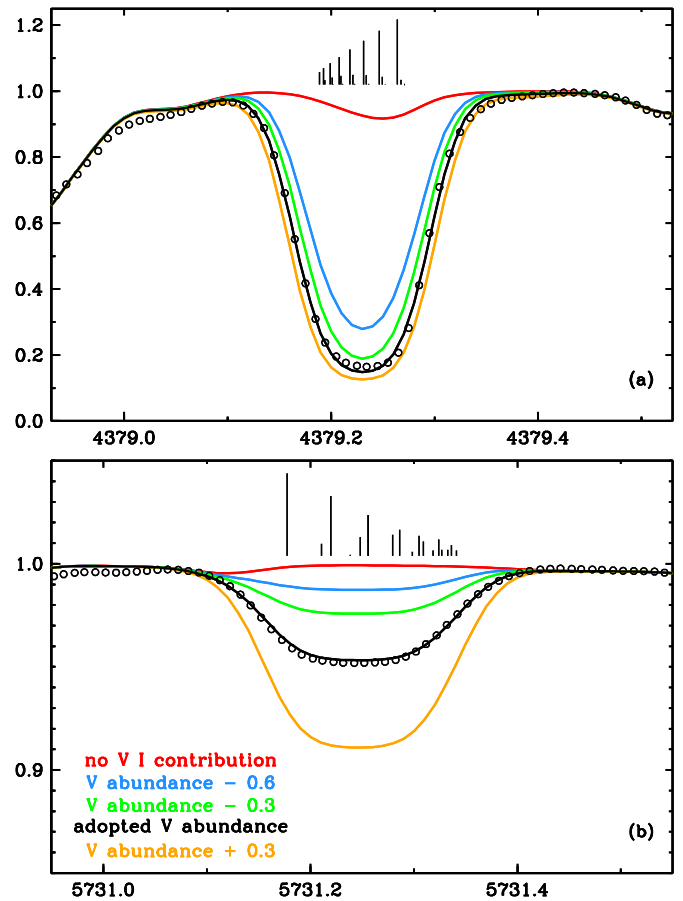
Figure 4. Synthetic and observed photospheric spectra of two V I lines with wide hyperfine substructure. For each transition, the vertical lines indicate the wavelengths and relative strengths of the 21 hyperfine components that make up the 4379.23 Å line (panel a) and the 18 hyperfine components that make up the 5731.25 Å line (panel b). The component wavelengths and fractional contributions to the total transition probability of each V I feature are indicated by their horizontal positions and vertical lengths. The green open circles represent every fourth point from the Delbouille et al. (1973) solar center-of-disk spectrum.

(A color version of this figure is available in the online journal.)

Observed/synthetic line matching is a better analytical technique even for weak V I lines.

As mentioned in Section 4, it is not possible to compute accurate HFS patterns for all useable solar V I lines. Some transitions (e.g., 4400.57, 6090.21, 6119.52 Å) have no detectable profile broadening in our very high-resolution laboratory spectra. For others (e.g., 4468.00, 5725.64 Å), some excess broadening of the laboratory line profile is present, but the effect is small and the line is on the weak-line part of the solar photospheric curve-of-growth (log(RW) < -5.5). In both of these cases we can treat the transitions as single lines with no loss of accuracy in derived abundance.

In Table 6, we give wavelengths, excitation energies, log(gf) values, and derived abundances for 93 V I solar photospheric lines. The final column of this table notes whether or not hyperfine substructure has been included in the abundance computations. For those lines with full hyperfine consideration, this column simply says "HFS." For those lines that are treated as single absorbers, we write "NO HFS" and also give the photospheric EW measured by Moore et al. (1966). These EWs show that many of the NO HFS lines are very weak (log(RW) $\leqslant$ -5.5, or EW $\leqslant$ 15 mÅ), and their EWs are not sensitive to assumed microturbulent velocity. Stronger lines treated as single

Table 6
Vanadium Abundances from Individual Lines of V I in the Sun

Wavelength (Å)	E. P. (eV)	log(gf)	log ε(V)	HFS?
3056.3328	0.017	0.05	3.95	HFS
3060.4522	0.040	0.21	3.92	HFS
3207.4072	0.069	−0.47	3.99	NO HFS; 30 mÅ
3400.3920	1.080	−0.58	4.10	HFS
3533.6758	1.217	−0.03	3.96	HFS
3667.7379	2.038	0.37	3.96	NO HFS; 15 mÅ
3688.0682	0.286	−0.28	3.93	HFS
3690.2794	0.262	−0.44	3.87	HFS
3692.2194	0.275	−0.17	3.88	HFS
3695.8647	0.267	−0.29	3.84	HFS
3704.6999	0.286	−0.02	3.85	NO HFS; 46 mÅ
3705.0332	0.275	−0.46	3.85	NO HFS; 33 mÅ
3808.5188	0.000	−0.90	3.94	HFS
3823.2121	0.275	−0.84	3.93	NO HFS; 25 mÅ
4050.9537	2.129	0.24	3.98	HFS
4095.4749	1.063	−0.11	3.98	NO HFS; 20 mÅ
4099.7833	0.275	−0.10	3.93	HFS
4105.1570	0.267	−0.14	3.94	HFS
4111.7788	0.300	0.40	3.92	HFS
4115.1768	0.286	0.05	3.95	HFS
4116.4716	0.275	−0.48	3.93	HFS
4116.5472	0.262	−0.85	3.96	NO HFS; 35 mÅ
4182.5824	0.275	−1.59	3.93	HFS
4232.4564	1.954	0.24	3.99	HFS
4379.2304	0.300	0.58	3.93	HFS
4400.5717	0.262	−0.39	3.93	NO HFS; 51 mÅ
4408.1958	0.275	−0.05	3.93	HFS
4412.1369	0.262	−1.58	3.94	NO HFS; 8 mÅ
4419.9337	0.275	−1.54	3.94	HFS
4421.5674	0.275	−0.81	3.96	NO HFS; 35 mÅ
4437.8304	0.286	−0.71	3.97	HFS
4444.2059	0.267	−0.76	3.93	HFS
4452.0051	1.866	0.59	3.98	HFS
4468.0001	1.847	−0.28	3.99	NO HFS; 10 mÅ
4560.7118	1.948	0.24	3.92	NO HFS; 8 mÅ
4577.1740	0.000	−1.08	3.98	HFS
4586.3660	0.040	−0.79	3.98	HFS
4594.1158	0.069	−0.66	3.97	HFS
4619.7771	0.040	−1.79	3.97	HFS
4635.1738	0.069	−1.92	3.95	HFS
4710.5525	2.129	−0.19	3.93	NO HFS; 4 mÅ
4807.5226	2.123	0.31	3.96	HFS
4827.4529	0.040	−1.47	3.92	HFS
4831.6462	0.017	−1.38	3.96	HFS
4832.4237	0.000	−1.50	3.96	HFS
4864.7298	0.017	−0.96	3.92	HFS
4875.4859	0.040	−0.79	3.94	HFS
4881.5569	0.069	−0.64	3.95	HFS
4900.6260	2.614	0.20	3.93	NO HFS; 3 mÅ
5234.0727	2.357	0.11	3.96	HFS
5584.4973	1.063	−1.18	3.96	HFS
5592.4148	1.050	−1.11	3.99	HFS
5604.9354	1.042	−1.26	3.95	HFS
5624.8741	1.050	−1.05	3.95	HFS
5627.6298	1.080	−0.35	3.98	HFS
5646.1074	1.050	−1.21	3.98	HFS
5657.4404	1.063	−1.00	3.96	HFS
5668.3618	1.080	−1.01	3.98	HFS
5670.8480	1.080	−0.43	3.99	HFS
5698.5189	1.063	−0.12	4.00	HFS
5703.5750	1.050	−0.21	3.98	HFS
5725.6386	2.364	−0.17	3.97	NO HFS; 2 mÅ
5727.0445	1.080	−0.02	3.98	HFS
5727.6551	1.050	−0.85	3.98	HFS
5731.2490	1.063	−0.74	3.97	HFS

Table 6
(Continued)

| Wavelength (Å)	E. P. (eV)	log(gf)	log ε(V)	HFS?
5737.0616	1.063	−0.74	3.99	HFS
5743.4377	1.080	−0.98	4.00	HFS
5772.4119	1.929	−0.55	3.93	NO HFS; 3 mÅ
6002.3026	1.217	−1.79	3.93	HFS
6002.6241	1.050	−1.57	3.93	weak, blended
6039.7256	1.063	−0.65	4.01	NO HFS; 11 mÅ
6058.1420	1.042	−1.40	3.98	HFS
6081.4422	1.050	−0.61	3.97	HFS
6090.2084	1.080	−0.07	3.99	NO HFS; 29 mÅ
6111.6506	1.042	−0.74	3.99	HFS
6119.5275	1.063	−0.36	3.98	NO HFS; 20 mÅ
6135.3650	1.050	−0.76	3.97	HFS
6199.1910	0.286	−1.46	4.04	HFS
6242.8216	0.262	−1.59	3.97	HFS
6243.1073	0.300	−0.94	3.95	HFS
6251.8231	0.286	−1.37	3.98	HFS
6256.9003	0.275	−2.02	3.93	HFS
6274.6524	0.267	−1.70	3.98	NO HFS; 6 mÅ
6285.1603	0.275	−1.54	3.97	NO HFS; 7 mÅ
6292.8244	0.286	−1.49	3.98	NO HFS; 9 mÅ
6296.4909	0.300	−1.61	3.96	NO HFS; 6 mÅ
6326.8357	1.866	−0.76	4.00	NO HFS; 2 mÅ
6349.4731	1.852	−0.95	3.98	NO HFS; 3 mÅ
6357.2913	1.847	−1.06	3.98	NO HFS; 2 mÅ
6531.4207	1.217	−0.85	3.96	HFS
6543.5037	1.194	−1.71	3.95	HFS
6624.8451	1.217	−1.30	3.93	HFS
9046.6926	1.194	−2.02	3.91	HFS
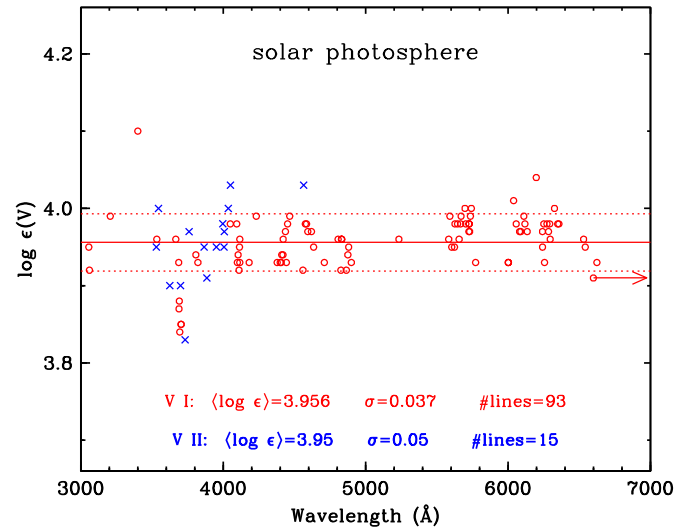
Figure 5. Vanadium abundances in the solar photosphere derived from V I lines (red circles) and V II lines (blue × symbols; Wood et al. 2014a) plotted as a function of wavelength. The abundance statistics for both species are given in the figure legend. The solid red line denotes the mean abundance derived from V I lines, and the dotted red lines denote the sample standard deviations ±σ. The red horizontal arrow indicates the abundance derived from the 9046.6 Å line. Since this is the only line in our solar abundance list that lies redward of 6625 Å, we have truncated the wavelength axis of the plot at 7000 Å to display the other lines more clearly.

(A color version of this figure is available in the online journal.)

absorbers typically have little or no detectable substructure in our lab spectra; these include the 3705.03 and 4400.57 Å lines.

The derived abundances are plotted as functions of wavelength in Figure 5 and excitation energy in Figure 6. These
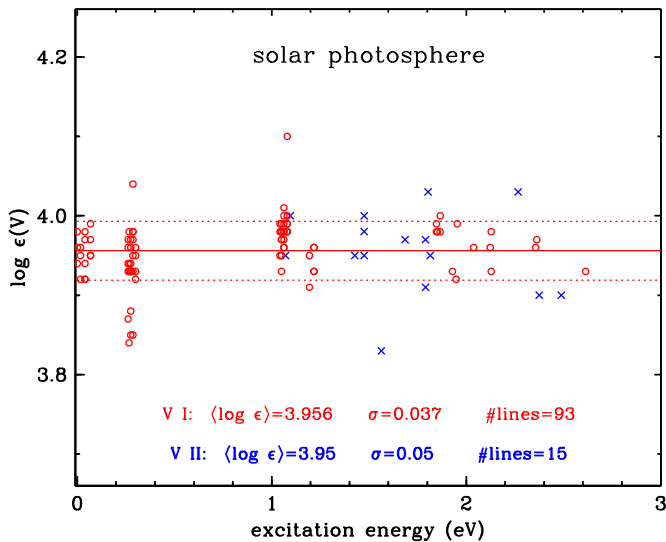
Figure 6. Vanadium abundances in the solar photosphere derived from V I and V II lines, this time plotted as a function of lower excitation energy. All symbols and lines are as in Figure 5.

(A color version of this figure is available in the online journal.)

figures also include the results for V II from Wood et al. (2014a). There are no significant trends of abundance with line wavelength, excitation energy, transition probability, or overall line strength. We note one exception that can easily be seen in Figure 5: five V I and one V II lines yield solar abundances that are about 0.1 dex smaller than all other transitions. These deviant lines all arise near 3700 Å, the wavelength region in which the higher Balmer-series hydrogen lines (H16 and greater) are piling up. The overlapping wings of these Balmer lines significantly affect the local "continuum" seen by the absorption lines. Our synthetic spectrum calculations take the Balmer absorption into account to first order, but better analyses need to be done in the future of the V I and V II lines in this spectral region. As such, our results for these five deviant transitions should be viewed with caution.

The mean photospheric V abundance derived from all 93 V I lines is $\log \varepsilon(\mathrm{V}) = 3.956 \pm 0.004$ ($\sigma = 0.037$). This value is in good agreement with the abundance from V II lines by Wood et al.: $\log \varepsilon(\mathrm{V}) = 3.95 \pm 0.01$ ($\sigma = 0.05$; 15 lines). The V I and V II photospheric abundances are also in excellent agreement with the meteoritic value recommended by Scott et al. (2014): $\log \varepsilon(\mathrm{V}) = 3.96 \pm 0.02$.

The internal line-to-line V I abundance scatter is so small that the real abundance uncertainty is a result of model solar atmosphere choice and analytical technique. Scott et al. (2014) have investigated these abundance effects for Fe-group neutral and ionized species in the solar photosphere. They suggest that abundances derived from V I lines with assumption of LTE are probably too low by 0.1 dex based on detailed calculations of other neutral species of other Fe-group elements. However, they caution that a thorough investigation of V I line formation is needed prior to definitive statements about the size of non-LTE effects. Scott et al. conclude by recommending $\log \varepsilon(\mathrm{V}) = 3.89 \pm 0.08$, giving the most weight to their 3D model photosphere computations. However, their LTE abundance from V I is $\langle \log \varepsilon(\mathrm{V}) \rangle = 3.97$ ($\sigma = 0.02$ from 30 lines), which is an identical result to ours for the 28 lines in common between the two studies. We re-derived the solar abundances of several V I lines with MARCS (Gustafsson et al. 2008) and ATLAS (Kurucz 2011) interpolated solar model atmospheres, and found

them to be about 0.04 dex smaller than those determined using the Holweger & Müller (1974) empirical model atmosphere. Exploration of full solar V abundance uncertainties that include the effects of more complete statistical equilibrium modeling assumptions is beyond the scope of this paper; see Scott et al. (2014) for further discussion.

6. THE VANADIUM ABUNDANCE OF METAL-POOR STAR HD 84937

Following our earlier papers on other Fe-group species, we apply the new laboratory V I data to the spectrum of the metal-poor main-sequence turnoff star HD 84937. This study continues our efforts to improve transition data for species that can be indicators for early Galactic nucleosynthesis (e.g., Kobayashi et al. 2006 and references therein). We are especially interested in the detection of both neutral and first ion species of Fe-group elements, in an attempt to separate real abundance effects from stellar atmosphere modeling and line formation effects. HD 84937 is chosen as the example star because of its favorable parameters: $T_{\mathrm{eff}} = 6300$ K, $\log g = 4.0$, [Fe/H] = −2.15, and $v_t = 1.5$ km s^{-1}. The relatively high temperature and gravity of this star ensure that H minus is the dominant continuous opacity source in nearly all spectral regions, and suggest that collisional excitation and ionization processes will be more important than radiative processes in V I energy level populations.

The chief problem in deriving abundances from V I lines in HD 84937 is simply one of detection. To our knowledge, lines of this species have never been analyzed in HD 84937. In Section 5 we discussed the lack of many very strong lines of V I in the solar spectrum. The low metallicity of HD 84937 creates challenges in even detecting V I features, much less deriving reliable abundances from them.

To illustrate this problem, consider the 4379.23 Å transition. The combination of low excitation energy, $\chi = 0.30$ eV, and large transition probability, $\log(gf) = +0.58$, combine to make it the sixth strongest (STR = +0.28) of our 836 V I lines. Moore et al. (1966) report, and we concur, that EW = 110 mÅ, or $\log(\mathrm{RW}) = -4.60$, in the solar photosphere. We derive a solar abundance for this line (Table 6) that is in good agreement with the mean value, and we can predict its strength in HD 84937. Adopting a model interpolated from the Kurucz (2011)[9] stellar photosphere grid with the parameters given above, we predict that if [V/Fe] = 0 then EW(4379Å) ≈ 4.5 mÅ, or log(RW) ≈ −6.0. Then from the *ESO VLT UVES* spectrum used in earlier papers of this series and described by Lawler et al. (2013), we measure EW ≈ 4.2 mÅ, very close to the predicted value. Thus it is not surprising that the literature on HD 84937 (e.g., Fulbright 2000; Gratton et al. 2003) contains no V abundance from V I lines.

We search our UVES spectrum for the strongest transitions of V I, and succeed in detecting 11 of them.[10] Absorption features in the HD 84937 spectrum are always present at the wavelengths of strong V I transitions. Two out of the 11 detected lines prove to be too weak for reliable abundance extraction. For the remaining nine features we determine V abundances from synthetic/observed spectrum matching. These abundances are listed in Table 7. Because the detected lines are extremely weak, we show all of them in Figure 7. We quote abundances only to the nearest 0.05 dex in Table 7, but the derived values are

---

[9] http://kurucz.harvard.edu/grids.html
[10] The 3183.96 and 3184.01 Å lines cannot be separated on our spectra, and thus are counted as one detected feature.
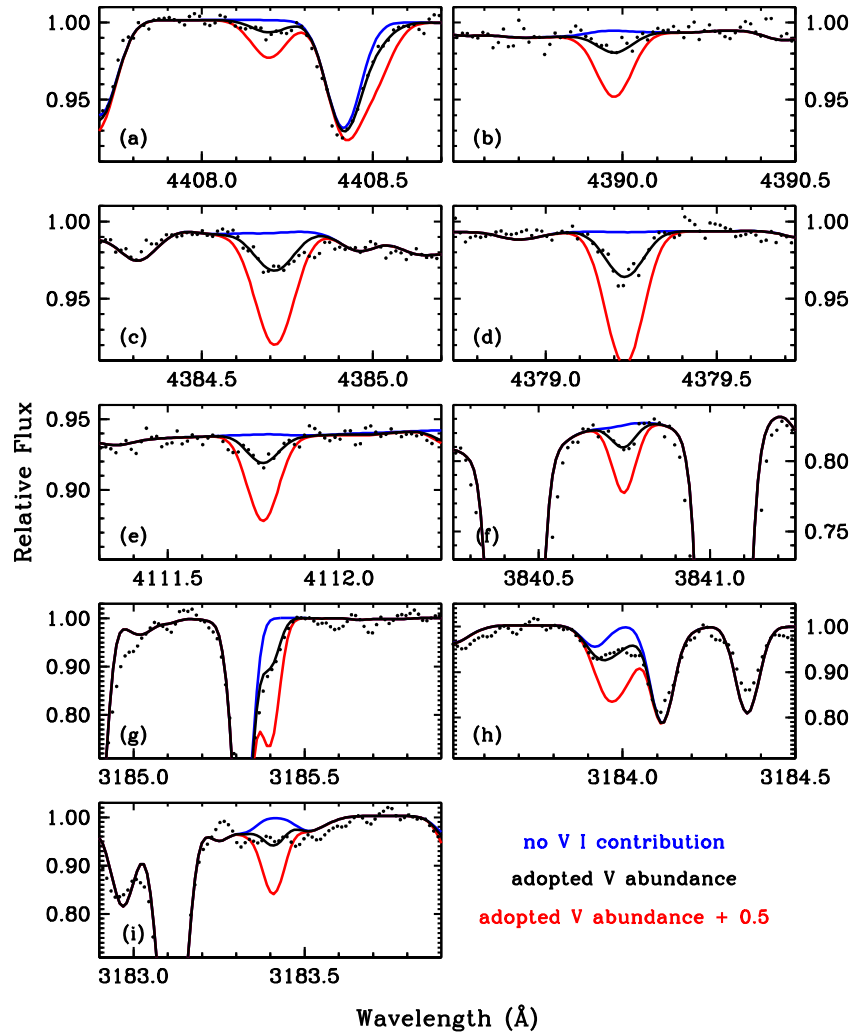
Figure 7. Observed and computed spectra for the nine V I lines used to derive the V abundance in HD 84937. The observed points are displayed as small filled circles, and the meanings of the red, black, and blue lines are given in the figure legend. In each panel, the "adopted V abundance" indicates the abundance derived for that particular V I feature (Table 7).

(A color version of this figure is available in the online journal.)

Table 7
Vanadium Abundances from Individual Lines of V I
in the Metal-poor Star HD 84937

| λ (Å)	χ (eV)	log(gf)	log ε	HFS?
3183.41	0.017	0.49	1.85	HFS
3183.96[a]	0.040	0.63	} 1.85	HFS
3184.01[a]	0.000	0.36		HFS
3185.40	0.069	0.73	1.95	HFS, Fe blend
3840.75	0.040	−0.16	2.05	Detection
4111.78	0.300	0.40	1.85	HFS
4379.23	0.300	0.58	1.85	HFS
4384.71	0.286	0.41	1.95	HFS
4389.98	0.275	0.22	1.85	Detection
4408.19	0.275	−0.05	1.85	Detection

Note. [a] The lines at 3183.96 Å and 3184.01 Å are blended in the stellar spectrum and are synthesized together.

consistent with each other to within uncertainties mostly driven by the signal to noise of the observed spectrum. We find a mean abundance from these nine V I lines of $\langle \log \varepsilon(V) \rangle = 1.89 \pm 0.02$ ($\sigma = 0.07$).

The individual line abundances in HD 84937 are plotted as functions of wavelength in Figure 8. We add to this figure the abundances from V II lines determined Wood et al. (2014a). Comparing this figure with Figure 5 for the solar photosphere, it is clear that V I and V II yield the same V abundances in each star. However, the tally of analyzed lines is lopsidedly in favor of V I in the solar spectrum and V II in the spectrum of HD 84937. We emphasize this difference in Figure 8 by showing the abundance mean and standard deviation lines for V II instead of V I. The ionized species result (Wood et al.) is obviously preferred here, but there is no evidence of a clash between the abundances derived from neutral and ionized transitions for this star.

The Wood et al. (2014a) study included V II lines in the vacuum UV spectral region of HD 84937. These lines appear in an *HST*/*STIS* UV high-resolution spectrum[11] of the star; see Lawler et al. (2013) for further description of that spectrum. However, that spectrum is not useful for the present study. The V I lines with $\lambda < 3000$ Å are not strong. All but one of them has STR ⩽ −0.5. This intrinsic transition weakness combines

---

[11] Obtained from the *HST* archive; the spectrum was gathered originally under proposal #7402 (P.I.: R. C. Peterson).
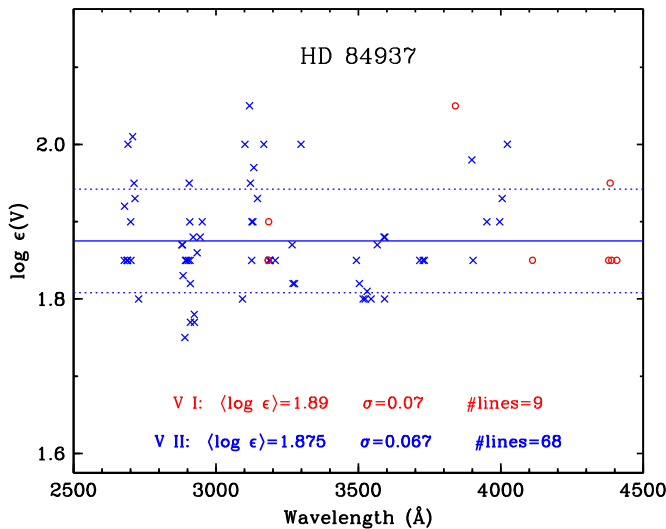
Figure 8. Vanadium abundances in HD 84937 derived from V I lines (red circles) and V II lines (blue × symbols; Wood et al. 2014a) plotted as a function of wavelength. The abundance statistics for both species are given in the Figure legend. The solid blue line denotes the mean abundance derived from V II lines, and the dotted blue lines denote the sample standard deviations $\pm\sigma$.

(A color version of this figure is available in the online journal.)

with the lower resolution and S/N of the STIS spectrum to yield lines that are undetectable.

The new V I determinations of $\log \varepsilon(V) = 3.96$ and 1.89 for the Sun and HD 84397 in conjunction with [Fe/H] = –2.32 (see Wood et al. 2014a) yield a value of [V/Fe] = 0.25 for HD 84397. Even though there are fewer V I lines available for such an abundance determination, this value is the same, within the error uncertainties, as the value found employing V II (Wood et al. 2014a). The iron-peak abundances place constraints on supernova models, particularly at early times in Galactic history. In the past, such models have suggested solar values for iron-peak-element/iron abundances. Our new precise value for [V/Fe] in HD 84397 at [Fe/H] = –2.32 (based upon both V II and V I) is clearly above solar and suggests a rise at lower metallicities. Examination of recent new data from Roederer et al. (2014) supports this contention, albeit with significant scatter (see Figure 8 in Wood et al. 2014a). However, additional high-quality data and theoretical model analysis will be required to understand the Galactic chemical evolution of V, and other iron-peak elements. Such a study is now in preparation.

7. SUMMARY

New emission branching fractions from FTS and echelle spectrometer data are used in combination with radiative lifetimes from LIF measurements (Den Hartog et al. 2014) to determine accurate, absolute atomic transition probabilities for 836 lines of V I. Complete HFS line component patterns for 94 lines of V I found useful in abundance studies are determined from the best published HFS A and B coefficients along with 26 HFS A coefficients from this study. Applications of these new data yield V abundance values in the Sun and metal-poor star HD 84937 of $\log \varepsilon(V) = 3.956 \pm 0.004$ ($\sigma = 0.037$) based on 93 V I lines and $\log \varepsilon(V) = 1.89 \pm 0.03$ ($\sigma = 0.07$) based on nine V I lines, respectively, both using the Holweger–Müller 1D model and in very good agreement with recent abundance values from lines of V II (Wood et al. 2014a). The resulting value of [V/Fe] = 0.25 supports a rise of V/Fe at low metallicity.

Note added is proof. After submission of this manuscript a new independent set of hyperfine structure constants for high-lying odd parity levels of neutral V was reported (Güzelçimen et al. 2014). These results agree with our results in Table 4 to within a small fraction of an error bar for levels in common.

REFERENCES

Adams, D. L., & Whaling, W. 1981, JOSA, 71, 1036
Asplund, M. 2005, ARA&A, 43, 481
Barklem, P. S., Christlieb, N., Beers, T. C., et al. 2005, A&A, 439, 129
Bonifacio, P., Spite, M., Cayrel, R., et al. 2009, A&A, 501, 519
Brault, J. W. 1976, JOSA, 66, 1081
Bridges, J. M., & Ott, W. R. 1977, ApOpt, 16, 367
Brooke, J. S. A., Bernath, P. F., Schmidt, T. W., & Bacskay, G. B. 2013, JQSRT, 124, 11
Brooke, J. S. A., Ram, R. S., Western, C. M., et al. 2014, ApJS, 210, 23
Cayrel, R., Depange, E., Spite, M., et al. 2004, A&A, 416, 1117
Childs, W. J., & Goodman, L. S. 1967, PhRv, 156, 64
Cochrane, E. C. A., Benton, D. M., Forest, D. H., & Griffith, J. A. R. 1998, JPhB, 31, 2203
Cowan, J. J., Sneden, C., Burles, S., et al. 2002, ApJ, 572, 861
Danzmann, K., & Kock, M. 1982, JOSA, 72, 1556
Den Hartog, E. A., Lawler, J. E., Sobeck, J. S., Sneden, C., & Cowan, J. J. 2011, ApJS, 194, 35
Den Hartog, E. A., Lawler, J. E., & Wood, M. P. 2014, ApJS, 215, 7
Delbouille, L., Roland, G., & Neven, L. 1973, Photometric Atlas of the Solar Spectrum from λ3000 to λ10000 (Liège: Inst. d'Ap., Univ. de Liège)
Doerr, A., Kock, M., Kwiatkowski, M., Werner, K., & Zimmerman, P. 1985, JQSRT, 33, 55
Fulbright, J. P. 2000, AJ, 120, 1841
GharibNezhad, E., Shayesteh, A., & Bernath, P. F. 2013, MNRAS, 432, 2043
Gough, D. S., Hannaford, P., Lowe, R. M., & Willis, A. P. 1985, JPhB, 18, 3895
Gratton, R. G., Carretta, E., Claudi, R., Lucatello, S., & Barbieri, M. 2003, A&A, 404, 187
Güzelçimen, F., Başar, Gö, Öztürk, I. K., et al. 2011, JPhB, 44, 215001
Güzelçimen, F., Ypaici, B., Er, A., et al. 2014, ApJS, 214, 9
Gustafsson, B., Edvardsson, B., Eriksson, K., et al. 2008, A&A, 486, 951
Hashiguchi, S., & Hasikuni, M. 1985, JPSJ, 54, 1290
Hinkle, K. H., Wallace, L., Ram, R. S., et al. 2013, ApJS, 207, 26
Holweger, H., & Müller, E. A. 1974, SoPh, 39, 19
King, R. B. 1947, ApJ, 105, 376
Kobayashi, C., Umeda, H., Nomoto, K., Tominaga, N., & Ohkubo, T. 2006, ApJ, 653, 1145
Kramida, A., Ralchenko, Yu., Reader, J., & NIST ASD Team (2013), NIST Atomic Spectra Database (ver. 5.1; Gaithersburg, MD: National Institute of Standards and Technology), Available: http://physics.nist.gov/asd [2014, August 6]
Kurucz, R. L. 2011, CaJPh, 89, 417
Lai, D. K., Bolte, M., Johnson, J. A., et al. 2008, ApJ, 681, 1524
Lawler, J. E., Bilty, K. A., & Den Hartog, E. A. 2011, JPhB, 44, 095001
Lawler, J. E., Bonvallet, G., & Sneden, C. 2001, ApJ, 556, 452
Lawler, J. E., Guzman, A., Wood, M. P., Sneden, C., & Cowan, J. J. 2013, ApJS, 205, 11
Lawler, J. E., Sneden, C., Cowan, J. J., Ivans, I. I., & Den Hartog, E. A. 2009, ApJS, 182, 51
Lefèbvre, P.-H., Garner, H.-P., & Biémont, E. 2002, PhyS, 66, 363
Masseron, T., Plez, B., Van Eck, S., Colin, R., Daoutidis, I., et al. 2014, A&A, in press
McWilliam, A. 1997, ARA&A, 35, 503
McWilliam, A., Preston, G. W., Sneden, C., & Searle, L. 1995a, AJ, 109, 2757
McWilliam, A., Preston, G. W., Sneden, C., & Shectman, S. 1995b, AJ, 109, 2736
Moore, C. E., Minnaert, M. G. J., & Houtgast, J. 1966, The Solar Spectrum 2935 Å to 8770 Å (NBS Monograph Vol. 61; Washington, DC: US GPO),
Ostrovskii, Yu. I., & Penkin, N. P. 1958 (Russ.), Opt. Spektrosk., 5, 345
Palmeri, P., Biémont, E., Aboussaïd, A., & Godefroid, M. 1995, JPhB, 28, 3741
Palmeri, P., Biémont, E., Quinet, P., et al. 1997, PhyS, 55, 586
Peck, E. R., & Reeder, K. 1972, JOSA, 62, 958

Ram, R. S., Brooke, J. S. A., Bernath, P. F., Sneden, C., & Lucatello, S. 2014, ApJS, 211, 5

Roederer, I. U. 2009, AJ, 137, 272

Roederer, I. U., Preston, G. W., Thompson, I. B., et al. 2014, AJ, 147, 136

Rudolph, J., & Herbig, V. 1982, JPhB, 15, L599

Scott, P., Asplund, M., Grevesse, N., Bergemann, M., & Jacques Sauval, A. 2014, arXiv:1405.0287

Sneden, C. 1973, ApJ, 184, 839

Sneden, C., Cowan, J. J., Lawler, J. E., et al. 2003, ApJ, 591, 936

Sneden, C., Lawler, J. E., Cowan, J. J., Ivans, I. I., & Den Hartog, E. A. 2009, ApJS, 182, 80

Sneden, C., Lucatello, S., Ram, R. S., Brooke, J. S. A, & Bernath, P. 2014, ApJS, 214, 26

Sobeck, J. S., Lawler, J. E., & Sneden, C. 2007, ApJ, 667, 1267

Suda, T., Yamada, S., Katsuna, Y., et al. 2011, MNRAS, 412, 843

Thorne, A. P., Pickering, J. C., & Semeniuk, J. I. 2011, ApJS, 192, 11

Thorne, A. P., Pickering, J. C., & Semeniuk, J. I. 2013, ApJS, 207, 13

Westin, J., Sneden, C., Gustafsson, B., & Cowan, J. J. 2000, ApJ, 530, 783

Whaling, W., Carle, M. T., & Pitt, M. L. 1993, JQSRT, 50, 7

Whaling, W., Hannaford, P., Lowe, R. M., et al. 1985, A&A, 153, 109

Wickliffe, M. E., Lawler, J. E., & Nave, G. 2000, JQSRT, 66, 363

Wood, M. P., & Lawler, J. E. 2012, ApOpt, 51, 8407

Wood, M. P., Lawler, J. E., Den Hartog, E. A., Sneden, C., & Cowan, J. J. 2014a, ApJS, 214, 18

Wood, M. P., Lawler, J. E., & Shetrone, M. D. 2014b, ApJL, 787, L16

Wood, M. P., Lawler, J. E., Sneden, C., & Cowan, J. J. 2013, ApJS, 208, 27

Wood, M. P., Lawler, J. E., Sneden, C., & Cowan, J. J. 2014c, ApJS, 211, 20

Woodgate, G. K. 1980, Elementary Atomic Structure (2nd ed.; Oxford: Clarendon Press), 184

Xu, H., Jiang, Z., & Lundberg, H. 2006, JOSAB, 23, 2597

Yong, D., Norris, J. E., Bessell, M. S., et al. 2013, ApJ, 762, 26